Joint Centre for Mesoscale Meteorology, Reading, UK

Contributions of the JCMM/ Dept of Meteorology Radar Group to 28th AMS Radar Meteorology Conference Austin, Texas, September 1997

Internal Report No. 70

July 1997

Met Office Joint Centre for Mesoscale Meteorology Department of Meteorology
University of Reading PO Box 243 Reading RG6 6BB United Kingdom
Tel: +44 (0)118 931 8425 Fax: +44 (0)118 931 8791
www.metoffice.com

Designed and produced by the Met Office © Crown copyright 2001 01/0240 The Met Office logo is a registered trademark.

CONTRIBUTIONS OF THE JCMM/DEPT OF METEOROLOGY

RADAR GROUP TO 28TH AMS RADAR METEOROLOGY CONFERENCE

AUSTIN, TEXAS SEPTEMBER 1997

1. Correction for severe attenuation at S-band.
T J Smyth and A J Illingworth
Suggests a polarimetric method for attenuation correction which should work at the operational C-band wavelength used in the UK network

2. Cirrus cloud ice water content retrieval algorithms for a future spaceborne cloud radar. Chun-Lei Liu and Anthony J Illingworth
Ice water content can be derived from radar reflectivity and ice temperature.

3. Examining the lower limit of Kdp rainrate estimation including a case study at S-band. T Mark Blackman and Anthony J Illingworth
Defines the lower rainfall limit for this new rainrate technique at S and C-band..

4. Estimating rainfall rates at the ground in bright band and non bright band events.
T J Smyth and A J Illingworth
Suggests *an extension to the Nimrod bright band algorithm so that the heavy rainfall rates of embedded convection are not reduced but are correctly estimated.*

5. Rainfall rate measurement with a polarimetric radar at an attenuated wavelength
Henri Sauvageot, Frederic Mesnard, Anthony Illingworth and John Goddard.
Demonstrates that a high frequency short range radar with a small antenna can be corrected for attenuation and used to measure rainrates.

6. Dual wavelength determination of cirrus microphysical properties.
Robin J Hogan, Anthony J Illingworth and Henri Sauvageot
A method for remotely sensing ice crystal size and more accurate water content.

7. A bistatic radar system using an incoherent transmitter
J.D.Eastment, T.M.Blackman, I.N.Moore and G.D.Aulich
A low cost method of implementing a dual Doppler radar.

1.2

CORRECTION FOR SEVERE ATTENUATION AT S-BAND

T.J.Smyth*and A.J.Illingworth
Department of Meteorology, Reading University, U.K.

1 INTRODUCTION

This paper presents observations made of a severe convective event on the 7th June 1996, which caused severe differential attenuation (A_{H-V}) of up to 5dB, by the S-band Chilbolton multi-parameter radar in Southern England. Rapid response raingauges, situated 500m below the precipitation region causing the attenuation, measured values in excess of 250mmhr^{-1}. A stable correction scheme is proposed which relies on both A_{H-V} and differential phase shift (ϕ_{DP}).

2 OBSERVATIONS

Figure 1 shows the differential attenuation (A_{H-V}) occurring behind a shaft of heavy rain as values of negative Z_{DR}. When "stripes" of negative Z_{DR} emanate from a region behind an intense rainfall shaft in a manner analogous to a shadow, this can show where attenuation is being caused. Two regions of A_{H-V} are apparent from figure 1 along the radials of 270° and 240°.

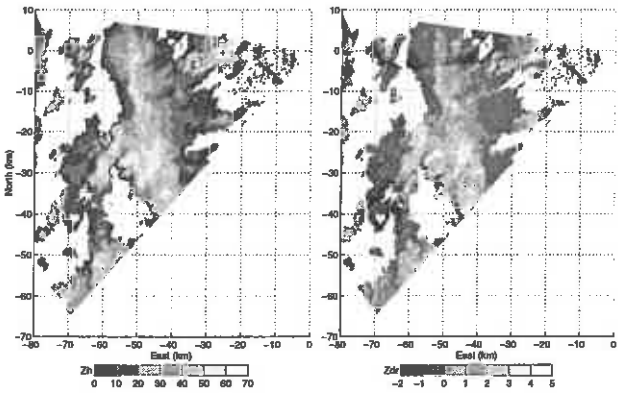

Figure 1: PPI of Z_H & Z_{DR} on 7/6/96 at 19:36:09GMT; g5 and g7 are raingauge positions.

3 THEORY

The radar response to hail and rain was modelled in terms of the scattering coefficients calculated using T-matrix code to predict the differential propagational phase shift (K_{DP},) the absolute attenuation (A_H), and (A_{H-V}). The scattering coefficients for hailstones of various structural compositions, i.e., dry, spongy (30% water-ice mixture), covered with a layer of water, were extracted using the T-matrix code and the effect of shape and alignment investigated. The concentration of the hailstones was modelled using the exponential dsd empirically derived by Cheng and English (1983). Figure 2 shows a comparison between the amounts of A_H resulting from spherical hailstones, and Marshall-Palmer (MP) rainfall. In rain at S-band, most attenuation is produced when Z_H >60dBZ. The hail contributes very little to the attenuation because it is present in such low concentrations. Because of these low concentrations, the K_{DP} of hail is much less than that of rain even if it is wet, aligned and oblate. To model the effect of rain, a

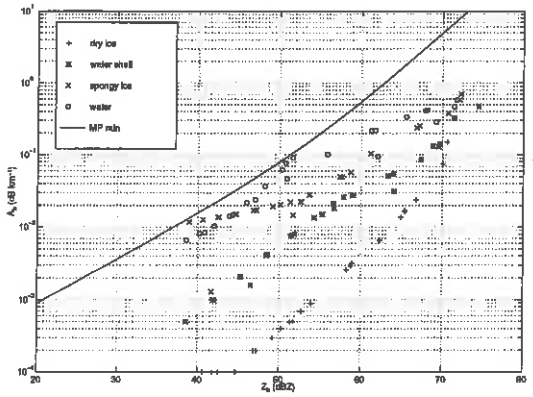

Figure 2: S-band comparison between hail and MP rain at 0°C.

normalised gamma drop size distribution (dsd) (equation 1) was used (Blackman, 1996) in preference to the gamma dsd and its associated relationships proposed by Ulbrich (1983).

$$N(D_e)dD_e = \frac{N_0}{|\mu|!}(\Lambda D_e)^{\mu} e^{-\Lambda D_e} dD_e \qquad (m^{-3}) \qquad (1)$$

$$\Lambda = \frac{(3.67+\mu)}{D_0} \qquad (mm^{-1}) \qquad (2)$$

where D_0 (mm) is the median diameter of the dsd, N_0 the concentration of the drops ($m^{-3}mm^{-1}$) and D_e their equivolumetric diameter; μ describing the form of the distribution. The shapes of Beard and Chuang (1987) were used. The use of the differential propagation phase shift (K_{DP}) to correct for attenuation has been proposed by (e.g.,Bringi *et al.*, 1990). They theoretically calculated linear relationships between K_{DP} and both A_H (solid line in figure 3) and A_{H-V}, (using the gamma dsd of Ulbrich (1983)) but truncated the values of D_0 at 2.5mm which is equivalent to a maximum Z_{DR} of 3dB. Higher values of Z_{DR} are frequently observed, so in this work D_0 is allowed to vary between 0 and 10mm and the spectrum truncated at 10mm. Temperature dependency is also an important factor, especially at S-band (Jameson, 1992), giving a 220% variation in the K_{DP} /A_{H-V} relationship between 0 and 30°C. Figure 3 (and a similar diagram for A_{H-V} against K_{DP}) show that the highest attenuation is caused by low concentrations of large drops.

4 CORRECTION SCHEME

The attenuation correction scheme which uses the two propagation observables, K_{DP} and the total amount of A_{H-V}, is outlined in figure 4. The total amount of A_{H-V} is estimated from the negative Z_{DR} beyond the intense precipitation and is partitioned amongst the gates where

*28th AMS Conference on Radar Meteorology, Austin, Texas, USA, Sept 1997

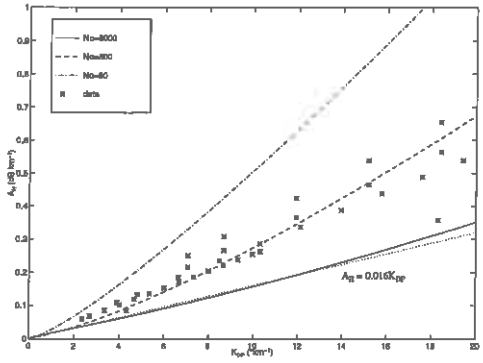

Figure 3: A_H as a function of K_{DP} for μ=0 (T=20°C). Data points are taken from the correction scheme values.

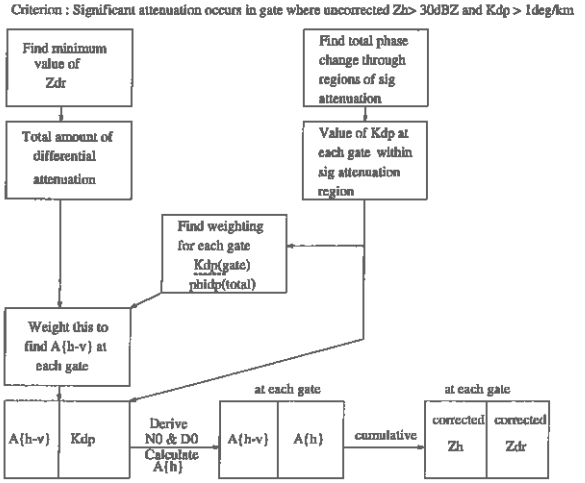

Figure 4: Flow diagram of the attenuation correction scheme.

K_{DP} >1° km^{-1} with a weighting proportional to the magnitude of K_{DP} . Values of N_0 and D_0 are derived from A_{H-V} and K_{DP} at each gate and A_H is computed. The corrected values of Z_H and Z_{DR} are then found from A_H and A_{H-V} at each gate. The highest values of attenuation occur in the regions of low N_0 and high D_0 and are only slightly affected by changes in the assumed value of μ.

5 VALIDATION

The extreme A_{H-V} of 5dB (at 19:06GMT) was caused by a region where Z_H and Z_{DR} were 67dBZ and 8dB (i.e., D_0 is very high) respectively, corresponding to a rain-rate (R) of 170mmhr^{-1} . This is the data point shown in figure 3 that has a K_{DP} of 15° km^{-1} and A_H of 0.5° km^{-1} . The model of Bringi *et al.*, which applies for $Z_{DR} \leq$3dB, would wrongly predict A_H to be only 0.25dBkm^{-1} . A_{H-V} is also underestimated. Figure 5 shows the attenuation algorithm applied to the ray passing over gauge 7 (32.2km) which recorded 3.3mmhr^{-1} . The attenuation occurred between 26 and 31.5km where K_{DP} values reached ~12° km^{-1} . The algorithm has corrected the 1.5dB loss in Z_{DR} shown at the furthest ranges. R calculated using the uncorrected Z_H and Z_{DR} is 7.9mmhr^{-1} over the location of gauge 7, whereas the corrected R=4.8mmhr^{-1} (both using μ=4). The correction for attenuation has lead to a reduction in the calculated R because the value of Z_{DR} has been increased, effectively reducing the number of small raindrops within the volume. The ray precisely over gauge 5 (Az 268.9° , not shown in figure 5) has Z_H =56dBZ and Z_{DR} =1.75dB giving R=268mmhr^{-1} which is in remarkable agreement with the 267mmhr^{-1} measured with the gauge.

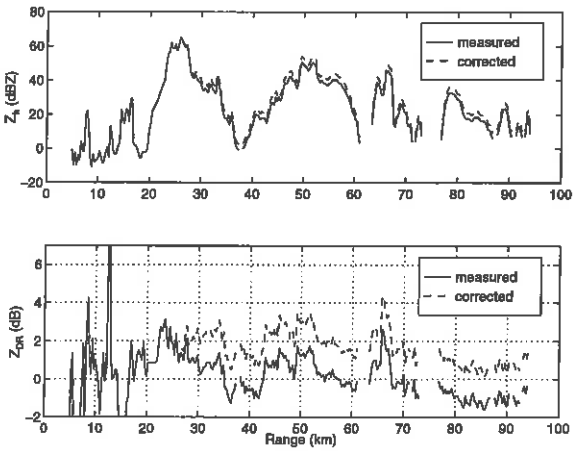

Figure 5: Attenuation correction algorithm implemented along ray Az 269.6° . Gauge 7 is situated at 32.2km.

6 CONCLUSIONS

Previously, attenuation correction schemes have relied upon gate-by-gate iterative methods which quickly become unstable. These methods also rely upon backscatter parameters such as Z_H and Z_{DR} which can become contaminated with hail within the volume. Hail is indistinguishable from rain when single parameter radar is used but should produce much less attenuation because of its low concentration. Therefore when hail is present the correction schemes may be needlessly implemented resulting in overcorrection. No such problems beset this method which uses both K_{DP} and A_{H-V} . Simpler methods using K_{DP} alone do not provide a unique solution.

ACKNOWLEDGEMENTS. Observations obtained as part of NERC "HYREX" program grant GST/02/718

5 REFERENCES

Beard, K. V. and Chuang, C. (1987). A new model for the equilibrium shape of raindrops. *J. Atmos. Sci.*, **44**, 1509–1524.

Blackman, T. M. (1996). *Observations and interpretations of differential phase shift in precipitation using S- and K_A-band radars.* Ph.D. thesis, Manchester University.

Bringi, V. N., Chandrasekar, V., Balakrishnan, N., and Zmić, D. S. (1990). An examination of propagation effects in rainfall on radar measurements at microwave frequencies. *J. Atmos. Oceanic Technol.*, **7**, 829–840.

Cheng, L. and English, M. (1983). A relationship between hailstone concentration and size. *J. Atmos. Sci.*, **40**, 204–213.

Jameson, A. R. (1992). The effect of temperature on attenuation-correction schemes in rain using polarization propagation differential phase shift. *J. Appl. Meteor.*, **31**, 1106–1118.

Ulbrich, C. W. (1983). Natural variations in the analytical form of the raindrop size distribution. *J. Climate Appl. Meteor.*, **22**, 1764–1775.

P1.34 CIRRUS CLOUD ICE WATER CONTENT RETRIEVAL ALGORITHMS FOR A FUTURE SPACEBORNE CLOUD RADAR

Chun-Lei Liu* and Anthony J. Illingworth
JCMM, Dept. of Meteorology, University of Reading, UK

1. INTRODUCTION

Cirrus clouds play a crucial role in the earth's radiation balance. Their importance in climate forecasting has been pointed out by Stephens *et al.* (1990). The positive or negative feedback of cirrus cloud on climate variation depends upon the ice particle effective diameter and ice water content (IWC). In order to validate the representation of cirrus clouds in present global models, data are needed on the global properties of cirrus clouds. Satellite are the only means to obtain global cloud statistics and radar is the only instrument which can penetrate clouds and provide vertical profiles of cloud properties. A planned future satellite should carry a cloud radar operating at one wavelength (about 3mm - 94 or 78GHz) and measure cloud reflectivity (Z) profiles. The reflectivity is proportional to ND^6, where N is cloud particle concentration and D is diameter. Models carry IWC which is proportional to ND^3. In this report, the cirrus cloud property retrieval algorithms are described for a future spaceborne cloud radar using the EUCREX (EUropean Cirrus and Radiation Experiment) and the CEPEX (Central Equatorial Pacific Experiment) aircraft data. There are about 14704 EUCREX and 12506 CEPEX spectra in our analysis, which are equivalent to 9200km and 7800km sampling distance, respectively.

2. RETRIEVING OF IWC

Assuming cirrus ice particle spherical and the exponential size spectra,

$$N(D) = N_o \exp(-\frac{D}{D^*}) \quad (1)$$

and an ice particle density

$$\rho = 0.07 D^{-1.1} \quad (2)$$

Using calculated Z (at 94GHz) and IWC from the observed spectra, Atlas *et al.* (1995) and Brown *et al.* (1995) have estimated IWC from Z for different D^* intervals (similar to Figure 1).

The temperature dependence of cirrus cloud ice particle size spectra has been investigated in earlier study of Heymsfield and Platt (1984) and recent study of Kosarev and Mazin (1991). They found that ice crystal size spectra observed at warmer temperatures tend to contain an increasing fraction of large particles, leading to higher values of D^*, Thus, it is conceivable that temperature might be used as a proxy for D^*. The cloud top temperature can be easily detected by meteorological satellite.

Following Brown *et al.* (1995), figure 1 shows the values of IWC and Z (at 94GHz) calculated from the EUCREX (Mid-Latitude Cirrus) aircraft data, and it is found that for an individual measurement of Z, the value of IWC retrieved is in error by about +100% and -50%.

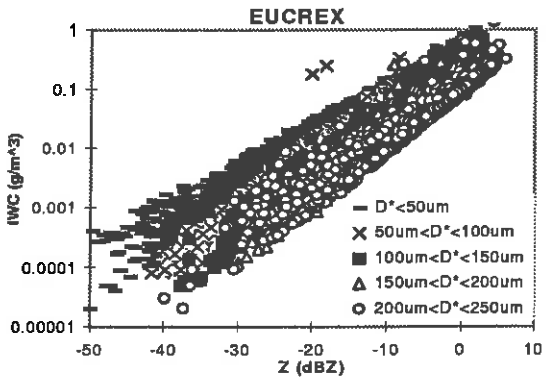

Figure 1: Scatter plot of IWC vs. Z. Different symbols represent different D* ranges.

If we could estimate the characteristic particle size D^*, e.g., by using the radar/lidar return signal (Intrieri *et al.*, 1993), then this would improve our IWC estimate. In figure 1, the data have been split up depending on the value range of D^*. The error in the value of IWC derived from a single measurement of Z is now reduced to about +40% and -30%. If the spectra were truly exponential then a knowledge of D^* and Z would give a perfect retrieval of IWC. However as we reduce the range of D^* we find the error does not fall further, this limit must be caused by deviations from exponentiality. In Figure 2 the data have been split up depending upon the range of temperature. The error on the value of IWC derived

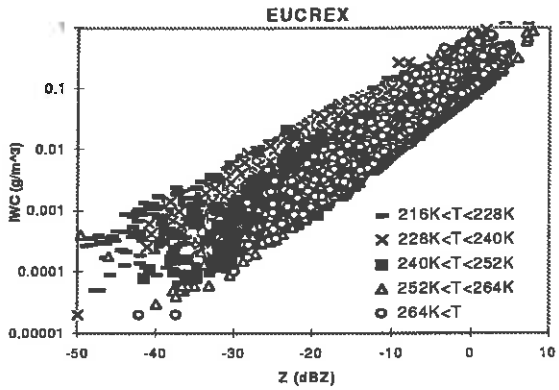

Figure 2: Scatter plot of IWC vs. Z. Different symbols represent different T (temperature) ranges.

* *Corresponding author address:*
Chun-Lei Liu, JCMM, Dept. of Meteorology,
University of Reading, Reading RG6 6BB, UK;
e-mail: swsliuc@met.rdg.ac.uk

from a single measurement of Z is now reduced to about +40% and -30%.

3. ERROR COMPARISON

In Figure 3, we compare the error (=one standard deviation σ) for EUCREX data sets in log(IWC) derived from a knowledge of Z and D^* with those from a knowledge of Z and T.

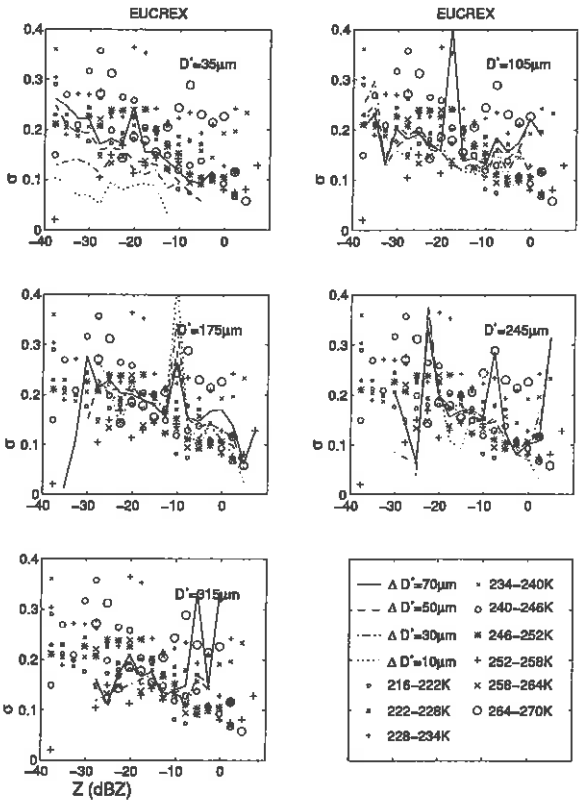

Figure 3: Error plot for EUCREX data. Symbols are from T classification and lines are from D^* classification.

Figure 3 attempts to quantify the comparative accuracy of classification of Z in terms of D^* or by T. The symbols representing the standard deviation for different temperature ranges, where the standard deviations in log(IWC) are derived from data subdivided for each 2.5dBZ step in Z and each 6K temperature step; these symbols are identical in each panel of the Figure. The separate panels are for the different central values of D^* with various line styles representing different widths of the class of D^* data deemed acceptable - in this figure the width of the class varies from 10 to 70μm around the central value. For example, the dotted line in the top left hand side of the figure represents a standard deviation of log(IWC) for all data with a D^* of 35±10μm.

The EUCREX data in Figure 3 reveal that the error using D^* and T are broadly comparable, and that increasing the spread of acceptable D^* only increases the standard error in the retrieved IWC by a small amount. The CEPEX data sets are also analyzed, results similar to figures 1 and 2 are found. Geographical bias usually less than 25%.

4. CONCLUSION

The value of IWC can be derived as accurately (+40%/-30%) from a knowledge of Z and T, as from using an additional instrument to estimate mean size. The +40%/-30% error in IWC from Z and D^* is introduced because of deviation of spectra from exponentiality. In any case deriving D^* would not be trivial; additional lidar measurements can be affected by crystal shape and density which introduce errors in lidar/radar backscatter ratio. In the future, we will use the multiwavelength ground based data and simultaneous aircraft validation of radar, to confirm the accuracy of deriving IWC derived from Z, T and D^*.

5. ACKNOWLEDGEMENTS

This work has been supported by NERC grant GR3/8765, ESTEC 10568/93 and CEC EV5V CT94-0463. We are grateful to Phil Brown and Andy Heymsfield who provided us EUCREX and CEPEX data sets.

6. REFERENCES

Atlas, D., S. Y. Matrosov, A. J. Heymsfield, M. D. Chou, and D. B. Wolff, 1995: Radar and radiation properties of ice clouds. *J. Appl. Meteor.*, **34**, 2329- 2345.

Brown, P. R. A., A. J. Illingworth, A. J. Heymsfield, G. M. McFarquhar, K. A. Browning and M. Gosset, 1995: The role of spaceborne millimeter-wave radar in global monitoring of ice cloud. *J. Appl. Meteor.*, **34**, 2346-2366.

Heymsfield, A. J., and C. M. R. Platt, 1995: A parameterization of the particle size spectrum of ice cloud in terms of ambient temperature and the ice water content. *J. Atmos. Sci.*, **41**, 846-855.

Intrieri, J. M., G. L. Stephens, W. L. Eberhard, and T. Uttal, 1993: A method for determining cirrus cloud particle size using lidar and radar backscatter technique. *J. Appl. Meteor.*, **32**, 1074-1082.

Kosarev, A. L., and I. P. Mazin, 1991: An empirical model of the physical structure of upper-layer clouds. *Atmos. Research*, **26**, 213-228.

Stephens, G. L., S. C. Tsay, P. W. Stackhouse, Jr., and P. J. Flatau, 1990: The relevance of the microphysical and radiative properties of cirrus clouds to climate and climatic feedback. *J. Atmos. Sci.*, **47**, 1742-1753.

3A.1 EXAMINING THE LOWER LIMIT OF K_{DP} RAINRATE ESTIMATION INCLUDING A CASE STUDY AT S-BAND.

T. Mark Blackman * Anthony J. Illingworth
JCMM, Univ. of Reading, Reading, UK

1. INTRODUCTION

The dual-polarization radar measurable K_{dp} (Doviak and Zrnic 1993) is increasingly interesting for robust rainrate estimation (Ryzhkov and Zrnic 1996), but current estimation schemes have significant measurement uncertainty compared to reflectivity-based estimates. Thus we seek to estimate the lowest measurable values of rainrate when using K_{dp} as a rainrate estimator.

2. ERROR ESTIMATION

Typical K_{dp} estimation schemes use a linear regression through a set of values of the measured ϕ_{dp} at consecutive range gates to estimate the gradient which should correspond to a measure of K_{dp} assuming that no backscattering differential phase shift δ is present. Bearing this in mind, we attempt to derive an approximate expression for the uncertainty in this estimate by starting from the basic principles associated with least squares fits. The first assumption is a constant uncertainty in the ϕ_{dp} data, σ_ϕ, and secondly that we use some number of points, N , with some fixed spacing (in range) between them, Δr.

The uncertainty in the estimated slope for this case may be shown to be

$$var(K_{dp}) = \sigma_b^2 = \frac{12}{N^3 - N}\left(\frac{\sigma_\phi}{\Delta r}\right)^2. \qquad (1)$$

If this is rewritten to illustrate the dependence of the total length the gradient estimate is derived over, $L = N\Delta r$,

$$var(K_{dp}) = \sigma_b^2 = \frac{12}{N - \frac{1}{N}}\left(\frac{\sigma_\phi}{L}\right)^2, \qquad (2)$$

then it becomes apparent that for fixed resolution scale of length L, the uncertainty, σ_b, varies inversely with $\sqrt{N}$ $(N \geq 2)$. If we assume as standard some unspecified power law relationship between specific differential phase shift K_{dp} and rainrate R, as

$$\text{two} - \text{way}\ \ K_{dp}\ \ (^\circ/km) = a\left(\frac{R}{1\ mm/hr}\right)^b \qquad (3)$$

then

$$\sigma_R \approx \frac{1}{ab}\left(\frac{R}{1\ mm/hr}\right)^{1-b}\sigma_b, \qquad (4)$$

we may use this to estimate the measurement error. For S-band we take $a = 0.12$, $b = 1.37$ and for C-band $a = 0.24$, $b = 1.37$ (Blackman and Illingworth 1995). Note that we treat the 1 mm/hr units conversion as assumed in further sections.

3. SPATIAL INTEGRATION

Clearly any estimate will improve with increasing integration over time and space. However these may not improve sufficiently over useful temporal and spatial scales. Figure 1 illustrates the geometry and variables involved. We then attempt to relate the uncertainty in each beam estimate of K_{dp} to the integrated rainrate estimate over the L-size box. After computing the K_{dp}

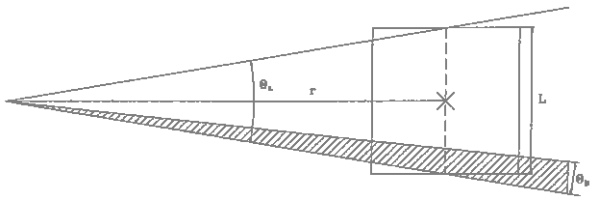

Figure 1: plan diagram illustrating spatial averaging possibility

in one beam over distance L, we perform further spatial integration by taking the mean rainrate estimate of m beams spread across the box shown in fig. 1. The integration "beamwidth", Θ_B, in this situation is defined as the distance the antenna traverses during the beam integration period. Note that this is *not* the beamwidth of the aerial, although it will closely correspond to it. The number of beams in a given box will depend therefore on the beamwidth (defined above, Θ_B) and the distance of the box from the radar. Following a trigonometric analysis of fig. 1 and the assumptions outlined we may estimate the number of beams, m, as

$$m = \frac{\Theta_L}{\Theta_B} = \frac{2\tan^{-1}(L/(2r))}{\Theta_B} \qquad (5)$$

With a couple of approximations not shown here we may then write,

$$\sigma_{\overline{R}} = \frac{\sigma_R}{\sqrt{m}} \qquad (6)$$

$$\sigma_{\overline{R}} = \frac{R^{1-b}}{ab\sqrt{m}}\sigma_{K_{dp}},$$

$$\sigma_{\overline{R}} \approx \frac{\sigma_\phi}{abR^{b-1}L^2}\sqrt{12\Theta_B r\Delta r}. \qquad (7)$$

For this form, σ_ϕ has units of degrees but Θ_B will be in radians, a has units of $^\circ/km$ if R has units of mm/hr, b is dimensionless, L and Δr have units of km.

*corresponding author address: Dept. of Meteorology, University of Reading, P.O. Box 243, Reading, UK. Tel. +44 (0) 118 987 5123 Fax. +44 (0) 118 931 8905 email: markb@met.reading.ac.uk

We may tabulate minimum expected values of $\sigma_{\overline{R}}$ for various (typical) values of L and r, and show the difference between S-band and C-band sensitivity to $\sigma_{K_{dp}}$. We have assumed $\sigma_\phi = 1.5°(\simeq$ minimum error for 64 pulse pairs, $0.2s$ integration),$\Delta r = 0.15km$ and $\Theta_B = 1.0°$. The other dependencies are indicated in table 1 which lists the minimum rainrates for which a measurement should not have an uncertainty larger than 25%, i.e. $\sigma_{\overline{R}} \leq 0.25\overline{R}$.

	Minimum Rainrate (mm/hr)					
L (km)	1.2	2.4	4.8	1.2	2.4	4.8
r (km)	S-band ($a = 0.012, b = 1.37$)			C-band ($a = 0.024, b = 1.37$)		
25	57	21	7.5	34	13	4.5
75	85	31	11	50	18	6.8
150	110	40	14	66	24	8.5

Table 1: Table indicating the minimum practically detectable rainrates for realistic radar and spatial integration parameters

5. CASE STUDY: 24 OCTOBER 1995

A narrow cold frontal rainband about 2km deep, with observed rainrates of $\approx 150mm/hr$ was observed embedded within a wide cold frontal rainband. This narrow but intense rainband passed over the fast ($30s$) response raingauges between 1820 and 1845 (depending on position.

We compared the performance of the three radar estimators, $R(Z)$,$R(Z, Z_{DR})$, and $R(K_{dp})$ w.r.t to the gauges at the same time. For each estimator we used a 1.2km box centred over each gauge to integrate the individual rainrate estimates over. For the purposes of this work, the only relevant quantity is the root-mean-square variation for the $R(K_{dp})$ estimator over the $1.2km$ box over the period 1630-1930 GMT on this day (24/10/95). This r.m.s. variation (during rainfall) as well as the anticipated value from the prior analysis is presented in table 2. Here we use $\sigma_\phi = 1.5°$,$N = 4$ and $\Delta r = 0.3km$ and $\Theta_B = 0.25$ for the Chilbolton S-band polarization-diversity radar.

The table (2) indicates that for this case the observed variation within the integration area agrees well with the predicted uncertainty on the basis of the preceding analysis and thus gives us confidence in our predictions about minimum observable rainrates.

6. CONCLUSION

Tables 1 and 2 reinforce the limited application of K_{dp} for small spatial scales and low rainrates. For example, 1° C-band radars at 1r.p.m and $1kHz$ PRF and a range of $150km$ with $2.4km$ resolution (needed for urban hydrology) can achieve 25% accuracy for $R > 24mm/hr$. In 'precipitation mode' NEXRAD systems (9 360° PPIs in $6min$) have $0.1s$ dwell time and equivalent $R > 40mm/hr$. However, in 'severe weather' mode, (14 PPIs in $5min$.) the 25% threshold limits use to even higher

Gauge	Radar Range (km)	Ang. Wid. of $1.2km$ box	Beams in box	Min. Uncert. (mm/hr) for given $\overline{R}$			Obs. r.m.s varn.
				2	20	60	
1	22	3.1	12	29	12	8	9.1
2	21	3.3	13	28	12	8	9.6
3	12	5.5	22	22	9	6	6.6
6	77	0.9	3	54	23	15	19.1
7	32	2.1	8	35	15	10	10.9

Table 2: Minimum K_{dp} Uncertainty Estimates Predicted/Observed for Each Rain-gauge for this rainfall event

rainrates. For these situations, Z or Z/Z_{DR} will always work better assuming no contamination due to hail and other ice precip. or ground clutter. K_{dp} should be insensitive to hail, but may be affected by differential phase shift on backscatter. The same insensitivity that allows K_{dp} to remain free of significant biases at high rainrates also ensures that it will not be useful at low rainrates. This also suggests that K_{dp} may be best used as a constraint on the more reflectivity-based measurements.

We also note that measurement uncertainties will usually be the largest errors. The physical errors are introduced primarily due to the use of staggered horizontal/vertical transmission schemes. This may potentially be avoided with the use of simultaneous horizontal/vertical transmit or with left/right circular polarization transmission. The efficacy of this approach would depend on what proportion of the phase uncertainty may be attributed to instrumental or physical effects.

7. ACKNOWLEDGEMENTS

We thank the staff at Chilbolton Observatory and at the RCRU, Rutherford-Appleton Laboratory for their invaluable assistance in obtaining these observations. Support was provided by NERC 'HYREX' grant GST/02/718.

References

Blackman, T. M. and A. J. Illingworth (1995). Improved measurements of rainfall using differential phase techniques. In *COST-75: Weather Radar Systems*, Luxembourg, pp. 814. European Commission.

Doviak, R. and D. Zrnic (1993). *Doppler Radar and Weather Observations* (2nd ed.). Academic Press.

Ryzhkov, A. and D. Zrnic (1996). Advantages of rain measurements using specific differential phase. *Journal of Oceanic and Atmospheric Technology 13*, 454–464.

3A.5

ESTIMATING RAINFALL RATES AT THE GROUND IN BRIGHT BAND AND NON-BRIGHT BAND EVENTS

T.J.Smyth* and A.J.Illingworth
JCMM, Department of Meteorology, Reading University, U.K.

1 INTRODUCTION

One of the major problems in estimating rainfall from a radar results from the change in reflectivity (Z) with height. As the range increases the radar beam is at a greater height and can either overestimate the rainfall if it intercepts the increased Z associated with melting snow ("the bright band" (BB)), or underestimate the rainfall if the beam is in the lower Z ice higher in the cloud (Joss and Waldvogel, 1990) . An operational scheme for correcting for such vertical profiles has been proposed by Kitchen *et al.* (1994). They use a climatological average profile (Illingworth, 1991) which has been derived from high resolution (0.25° beamwidth) data taken with the S-band RAL Chilbolton radar in Southern England. This profile (figure 1) has a constant value of Z (Zb) in the rainfall; the BB enhancement of Z is represented by a triangular profile of depth 700m and is related to Zb. Finally, the profile in the ice is fixed using the height of the

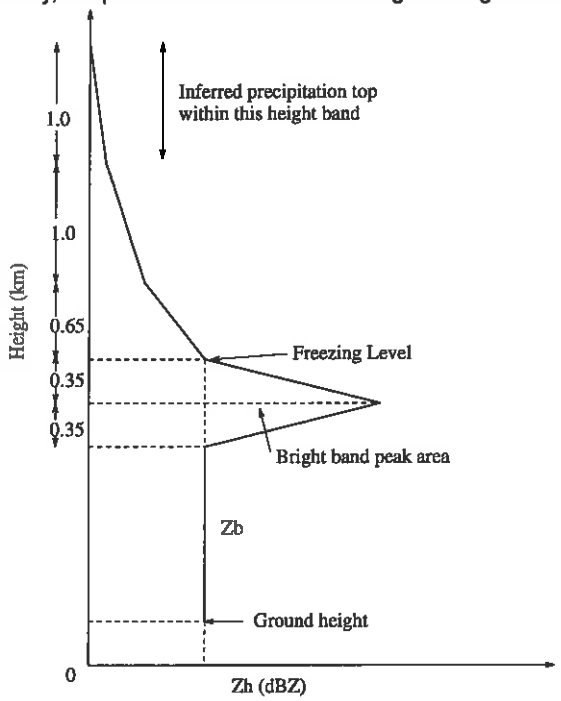

Figure 1: Idealised vertical profile

top of the echo. The correction is performed by first normalising the height of the profile so that the top of the BB coincides with the 0°C isotherm derived from an operational forecasting model. The second step in the correction is to scale the Z values of the profile so that the observed value of Z from the lowest elevation radar beam agrees with the value obtained by multiplying the profile by the beam pattern of the radar at that range. Validation in stratiform rainfall showed a significant improvement in rainfall estimates.

The next step in improving the corrections would appear to be to use higher elevation radar beams to provide a more accurate estimate of the Z gradient rather than using a climatological profile. However, when this was done (Kitchen, 1997) no further improvement could be detected, thus confirming the assertion of Fabry *et al.* (1992) that beyond the range where the radar horizon intercepts the freezing level, "any attempt to obtain quantitative rainfall estimates is futile."

The correction scheme of Kitchen *et al.* is always applied operationally in the UK Met. Office NIMROD algorithm, even for convective precipitation when BBs may be absent. In such cases if the lower radar beam intercepts a convective core near the freezing level, a BB would be wrongly diagnosed and the heavy rain underestimated. This could lead to errors in local flood predictions. Divjak (1994) calculated representative Z profiles averaged over an area from 5 to 60km around the radar and over a period of one hour. This representative was then divided into one of two classes: stratiform if the average Z gradient above the freezing level was above -2.5dBkm^{-1} , convective if it was less. The disadvantage of this method is that the same profile is applied to the whole radar scan, even when (as is usually the case) the convective cells are embedded in stratiform precipitation.

In this paper we examine the use of the Linear Depolarisation Ratio (LDR) for identifying the presence or absence of a BB, and compare the height estimate of the BB from LDR with the value in the numerical model. In addition, we compare vertical profiles (VP) when a BB is and is not present, and suggest a simple extension to the Kitchen *et al.* algorithm which should prevent the rainfall being underestimated when the BB is absent.

2 IDENTIFICATION OF THE BB FROM LDR

Observations made with the S-band polarisation diversity radar at Chilbolton show that high values of LDR are an excellent identifier of the BB. Comparisons with aircraft measurement (Frost *et al.*, 1991) showed that low density oblate melting snowflakes were associated with values of LDR of about -16dB, but that more spherical melting graupel pellets only resulted in LDR values of about -25dB. This is consistent with both types of ice tumbling randomly, but with the snowflakes having an average axial ratio of about 0.5 to 0.6, whereas that of the graupel pellets was about 0.8. An extensive comparison of VPs of Z and LDR has been made using RHIs from the Chilbolton radar. Three 300m range gates were averaged to give the VP, and data with a maximum range of 80km used so that the vertical resolution was better than 300m. It was found that a maximum value of LDR of >-18dB reliably indicated the presence of a BB, Accordingly, when low level PPIs are used to estimate rainfall

*28th AMS Conference on Radar Meteorology, Austin, Texas, USA, Sept 1997

over a large area, then the values of LDR above -18dB identify the presence of a BB.

In addition, on 8 days the height of the maxima in Z and LDR were compared with the value of the 0°C isotherm in the UK Meteorological Office Mesoscale Model. The model was run every three hours with forecasts available every hour. For all 22 comparisons made the LDR BB was always between 0 and 100m below the BB in Z. On 14 occasions the BB in Z was between 200 and 300m below the 0°C isotherms; on the other 6 it was about 100m below the isotherm. On one occasion the BB height changed by 200m over the 80km range of the RHI and the 0°C isotherm in the model reproduced this change.

It appears that the maximum value of LDR follows the height of the BB slightly more closely that the mesoscale model, but that the model performance is accurate enough. Harrold *et al.* (1968) have drawn attention to sudden changes in the height of the BB, however our experience with Chilbolton data indicates that this is quite rare and, in any case, if the model assimilates data and is run every three hours it should be able to cope with such changes. Installation of the LDR parameter requires only small changes to the radar receive electronics, and could be used for identifying the height of the BB if a mesoscale model is not available. Once the BB height is known from LDR, then the Kitchen *et al.* (1994) method of adjusting a standard profile to agree with observations should work. Further work is needed however to simulate the values of LDR at large distances when the BB does not fill the beamwidth of a 1° operational radar. In addition at C-band propagation effects can lead to a rise in LDR with range in heavy rain.

3 VERTICAL PROFILES WITH AND WITHOUT A BRIGHT BAND.

The mean values of VP for cases with and without a BB is displayed in figure 2; a maximum value of LDR of -18dB being used to differentiate the two classes. The profiles

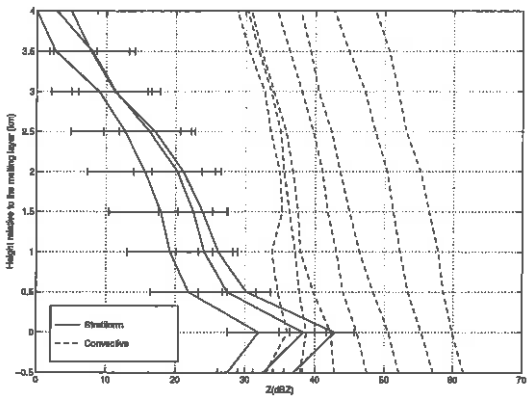

Figure 2: Contrast between severe convection (dashed) and stratiform (solid) vertical Z profiles

have been classified by the value of Z in the rain (Zb) and separated into bins of width 5dBZ, and for the stratiform cases the standard deviations of the dBZ is displayed. The analysis was made using 4059 convective profiles and 7892 stratiform profiles. The difference between the two different VP types is very clear. A simple modification to account for the absence of BBs in convective echoes would be to use a a criterion the magnitude of Z at 1.5km above the BB. If Z is above 30dBZ at the height, then the BB profile correction should be suppressed, and instead a profile in which the value of Z increases with falling distance by about 2dBkm^{-1} should be substituted. This criterion is presently undergoing operational trials.

Figure 2 shows the difficulty of predicting the rainfall at the ground in stratiform rainfall when the beam is above the BB. The three profiles for a mean Z in the rain of 30-35, 35-40 and 40-45dBZ are remarkably similar once the beam is over 1.5km above the BB.

4 CONCLUSIONS

1) BB correction works well in stratiform rainfall using 0°C isotherm of a mesoscale model to fix the height scale of a climatological profile, and then adjusting the magnitude of the profile to give the observed Z.
2) LDR also gives height of the BB to within 100m and could be useful if a mesoscale model is not available. Further validation is needed for C-band radars and at large ranges where the BB does not fill the beam.
3) BB correction schemes based on Z alone will fail when there is embedded convection which does not have a BB, but LDR will recognise such cases. A simple method for Z only radars could use a value of Z 1.5km above the BB. When this exceeds 30dBZ the BB correction should be suppressed, and instead a VP which shows a steady increase of Z of 2dBkm^{-1} with decreasing height should be used.
4) Accurate climatological values of mean profiles are needed. These may vary in different parts of the world, but in the UK at least there does not seem to be a seasonal variation.

ACKNOWLEDGEMENTS. Observations obtained as part of NERC "HYREX" program grant GST/02/718

5 *

5 REFERENCES

Divjak, M. (1994). Radar measurement of precipitation: The use of vertical reflectivity profiles. In *Cost 75*, pages 73–84, Brussels, Belgium.

Fabry, R., Austin, G. L., and Tees, D. (1992). The accuracy of rainfall estimates by radar as a function of range. *Quart. J. Roy. Meteor. Soc.*, **119**, 1427–1463.

Frost, I. R., Goddard, J. W. F., and Illingworth, A. J. (1991). Hydrometeor identification using cross polar radar measurements and aircraft verification. In *25th Conference on Radar Meteorology*, pages 658–661, Paris, France. Amer. Met. Soc.

Harrold, T. W., Browning, K. A., and Nicholls, J. M. (1968). Rapid changes in the height of the melting layer. *Meteorol. Mag*, **97**, 327–332.

Illingworth, A. J. (1991). Assessment of bright band correction procedures. Meteorological Office report.

Joss, J. and Waldvogel, A. (1990). *Radar in Meteorology. Ed. Atlas, D.*, chapter 29a: Precipitation, measurement and hydrology, a review, pages 577–606. AMS, Boston, 1st edition.

Kitchen, M. (1997). Towards improved radar estimates of surface precipitation. *Quart. J. Roy. Meteor. Soc.*, **123**, 145–163.

Kitchen, M., Brown, R., and Davies, A. G. (1994). Real-time correction of weather radar for the effects of bright band, range and orographic growth in widespread precipitation. *Quart. J. Roy. Meteor. Soc.*, **120**, 1231–

3A.7 RAINFALL RATE MEASUREMENT WITH A POLARIMETRIC RADAR AT AN ATTENUATED WAVELENGTH

Henri Sauvageot * and Frédéric Mesnard
Université Paul Sabatier, Laboratoire d'Aérologie, Toulouse, France

Anthony J. Illingworth
University of Reading, U.K.

John W. F. Goddard
Rutherford Appleton Laboratory, U.K.

1. INTRODUCTION

The causes of the errors affecting the radar rain measurement methods, derived from the polarimetric algorithm pioneered by Seliga and Bringi (1976), are mainly:

- the uncertainty on the radar calibration,
- the spatio-temporal variability of the drop size distribution (DSD), and
- the atmospheric attenuation, which is the sum of two terms: the attenuation by rain, that can be corrected when low but not when strong (Hildebrand, 1978), and the attenuation by water clouds, which is frequently ignored even when it is not negligible. For example at X band, a water cloud with a water content of 2 g m^{-3} produces the same attenuation as a rain of about 11 mm h^{-1}.

Sauvageot (1996) proposed an algorithm for rain rate measurement with a polarimetric radar, working at an attenuated wavelength. Theoretical arguments and numerical simulation show that this algorithm is:

- independent from a radar calibration,
- poorly influenced by the shape of the DSD,
- not biased by the attenuation by water clouds,
- able to qualitatively detect the anomalous propagations and the presence of hail.

The object of this paper is, after a brief recall on the attenuated polarimetric algorithm, to present an example of result from real data.

2. THE ATTENUATED POLARIMETRIC METHOD (APM)

The schematic of the APM is summed up in Figure 1. At attenuated wavelengths, the differential reflectivity for horizontal and vertical polarization, Z_{DR}, is the addition of a term depending on the drop shape, Z_{DRS}, and a term depending on the differential attenuation for the two polarizations, A_{DP}. The differential attenuation can be interpreted as an estimation of the integral of the rainrate along the radar beam. The principle of the method is the following: a first estimation of the rainrate R is calculated from the single wavelength radar reflectivity factor Z, using the usual iterative attenuation correction scheme (Hildebrand, 1978) and a combination of a Z-R and an A-R relation, where A is the single polarization attenuation coefficient by rain. This result enables the obtaining of an estimation of Z_{DRS}. The difference between the measured value of Z_{DR} and Z_{DRS} is a measure of A_{DP}. Then the integral of R along the radar beam, deduced from the single polarization reflectivities, is constrained to be equal to the integral of R deduced from A_{DP}. This constraint is used to adjust interatively the linear parameter of the Z-R relation (let α be this parameter), the other (β the power parameter) being maintained constant at a mean climatological value. The adjusted α enables the calculation of R in each gate. The radial observed with the radar can be partitioned and the algorithm applied independently to the individual segments with one value of α computed for each segment.

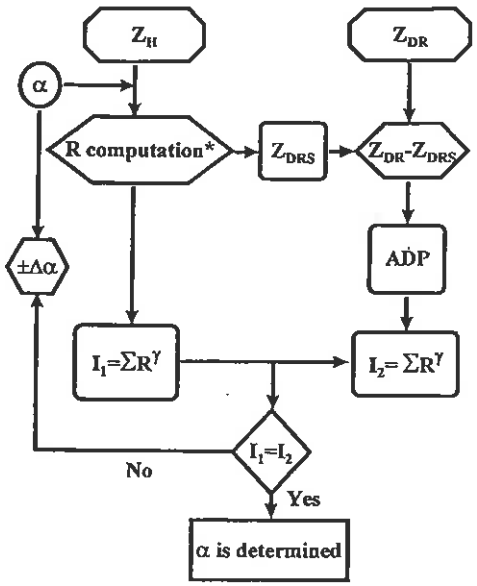

Figure 1. Schematic of the Attenuated Polarimetric Method. γ is the power coefficient of the A-R relation.

3. DATA

The correct way to test this algorithm consists in measuring rain rates and cumulative rain heights, using only a polarimetric radar, and in comparing the results with independent data obtained at the ground

* *Corresponding author address:* Dr. Henri Sauvageot, Université Paul Sabatier, Observatoire Midi-Pyrénées, Laboratoire d'Aérologie, 14 avenue Edouard Belin, 31400 Toulouse, France. e-mail: sauh@aero.obs-mip.fr

with a raingauge network. Such an experiment will be implemented in the near future with an X-band radar in France. A first attempt at verifying this method on real data was performed on the site of the Chilbolton radar observatory in UK, using two radars: 1) the Ka band (35 GHz) polarimetric radar RABELAIS as attenuated radar working with the APM and 2) the unattenuated S band (3 GHz) radar CAMRa, working with the simple Z-R algorithm, as a reference. The Ka band antenna is set on the side of the S band antenna enabling a direct ray by ray comparison. For CAMRa, owing to the huge antenna, the near-field area ranges up to about 6 km from the radar. The 3dB beamwidth is 0.4° and 0.2° for RABELAIS and CAMRa respectively. CAMRa is regularly calibrated against raingauges.

4. RESULTS

Figure 2 presents the case observed on July 26, 1995 at 0846 UTC. The curves shows the average over three contiguous radii with an azimuth between 69°40' to 70°20' and for a 0° elevation. The object of this averaging is to reduce a possible mismatching of the two beams due to the different beamwidths and to the side by side position. The range gates are 0.3 km from each other with the analysis starting at a distance of 6 km. Three curves are presented showing the rainfall rate R as a function of the distance. The dashed line (with the open squares) is the rain rate observed from the 3 GHz radar using a locally tuned Z-R relation. It is assumed to be closed to the real values (with possible gate to gate deviation owing to the DSD small scale variability). The dotted line (with crosses) is the rain rate observed with the 35 GHz radar. What can be seen is that the Ka band measurement is strongly attenuated in the first rain cell, between 6 and 10 km. Beyond 10 km, the information on the R distribution is ruined. After 16 km the signal is almost at extinction, the measured R is 0.1 and 0.05 mm h^{-1} at 16 km and at 17.8 km respectively. The unbroken line (with open squares) displays the 35 GHz rain rate after processing with the APM, without using any other piece of information. Some discrepancies with the 3 GHz rain rate are observed before 10 km (possibly due to beams mismatch). Beyond 10 km the attenuated polarimetric algorithm almost exactly retrieves the observation of the 3 GHz radar. The corrected attenuation at the end of the line is larger than 30 dB (from 0.05 to 4 mm h^{-1} that is, in term of reflectivity factor, from about 2 dBZ to 34 dBZ).

For the computation, we have used $\beta = 1.1$. This is the value computed by Wexler and Atlas (1963) at 35 GHz for Mie scattering and Marshall Palmer DSD at 0°C. The average α obtained using the APM in the case of Figure 2 is 504 (the three individual values are 518, 512 and 484). This value compares very well with that computed by Wexler and Atlas (1963) which is 450 for R between 5 and 20 mm h^{-1}.

The APM is able to retrieve the correct rain rate distribution as long as the radar signal is above the extinction level.

5. REFERENCES

Hildebrand, P.H., 1978: Iterative correction for attenuation of 5 cm radar in rain. *J. Appl. Meteor.*, **17**, 508-514.

Sauvageot, H., 1996: Polarimetric radar at attenuated wavelengths as a hydrological sensor. *J. Atmos. Oceanic Technol.*, **13**, 630-637.

Seliga, T.A., and V.N. Bringi, 1976: Potential use of radar differential reflectivity measurements at orthogonal polarizations for measuring precipitation. *J. Appl. Meteor.*, **15**, 69-76.

Wexler, R., and D. Atlas, 1963: Radar reflectivity and attenuation of rain. *J. Appl. Meteor.*, **2**, 276-280.

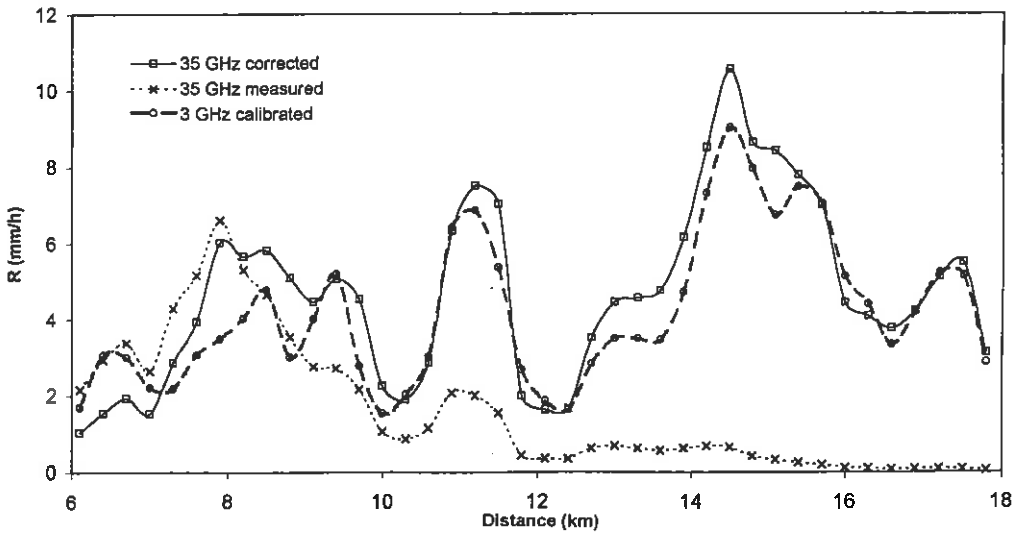

Figure 2. Rain rate R as a function of distance observed with the calibrated 3 GHz radar, with the attenuated 35 GHz radar and retrieved from 35 GHz using the APM with 8 iterations.

P3.31 DUAL WAVELENGTH DETERMINATION OF CIRRUS MICROPHYSICAL PROPERTIES

Robin J. Hogan,* Anthony J. Illingworth and Henri Sauvageot†

University of Reading, Berkshire, UK †Université Paul Sabatier, Toulouse, France

1 INTRODUCTION

Cirrus clouds play an important role in the earth's radiation budget, and consequently accurate representation of ice cloud properties in General Circulation Models is essential for reliable simulations of present and future climate. Systematic measurement of cloud parameters, particularly Ice Water Content (*IWC*) and effective radius (r_e), is required for model validation. The sensitivity of millimeter-wave radar presents us with a very useful tool in the study of clouds, but the natural variation in size distribution is such that empirical *Z–IWC* relationships are accurate to only +100% and –50% (Brown et al. 1996).

Results are presented from two coincident radars located at Chilbolton, England—the 35 GHz Rabelais and the 94 GHz ESTEC Galileo—which by comparison of reflectivities can provide size information (Matrosov 1993). As the size of the crystals increases, Mie scattering progressively reduces the 94 GHz reflectivity factor Z_{94} below the 35 GHz reflectivity factor Z_{35}, so that the Dual Wavelength Ratio, defined as $DWR = 10\log_{10}(Z_{35}/Z_{94})$, rises above 0 dB, its magnitude being a directly related to some measure of mean size, such as median volume diameter D_0.

We assume that ice crystals can be approximated as spheres for scattering purposes, and that their size spectra are described by an exponential distribution:

$$n(D) = N_0 \exp(-3.67D/D_0).$$

For crystals with diameters of less than 1 mm, we follow the findings of Brown and Francis (1995) and adopt a density of $\rho = 0.07D^{-1.1}\,\mathrm{g\,cm^{-3}}$ (up to a maximum of $0.917\,\mathrm{g\,cm^{-3}}$). It would seem unlikely however that larger crystals, which may well be growing by aggregation, should continue to decrease in density at this rate, but firm experimental evidence is scarce. We shall consider three functions for the density above 1 mm: (1) $\rho = 0.07D^{-1.1}$ as before, (2) $\rho = 0.07D^{-0.55}$, and (3) a constant value of $0.07\,\mathrm{g\,cm^{-3}}$. Mie scattering calculations have been carried out, and figure 1a shows *DWR* as a function of D_0 for each case. The size derived from *DWR* is clearly quite dependent on which density function is chosen. Ice Water Content is then given by $IWC = Z_{35}f(D_0)$, where

$$f(D_0) = \frac{\frac{\pi}{6}\int_0^{D_{max}} \rho D^3 \exp(-3.67D/D_0)\,dD}{\int_0^{D_{max}} \frac{|K(\rho)^2|}{0.93} D^6 \exp(-3.67D/D_0)\,\gamma_{35}(D)\,dD}$$

The distribution is truncated at $D_{max} = 5$ mm, and $\gamma_{35}(D)$ is the ratio of Mie to Rayleigh backscattered power for a crystal of diameter D at 35 GHz. A similar expression is

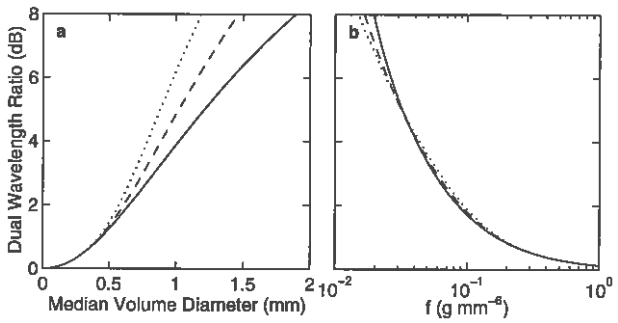

Figure 1: Dual Wavelength Ratio as a function of (a) median volume diameter D_0 and (b) the parameter f, for density functions 1, 2 and 3 (described in the text) shown by the solid, dashed and dotted lines respectively.

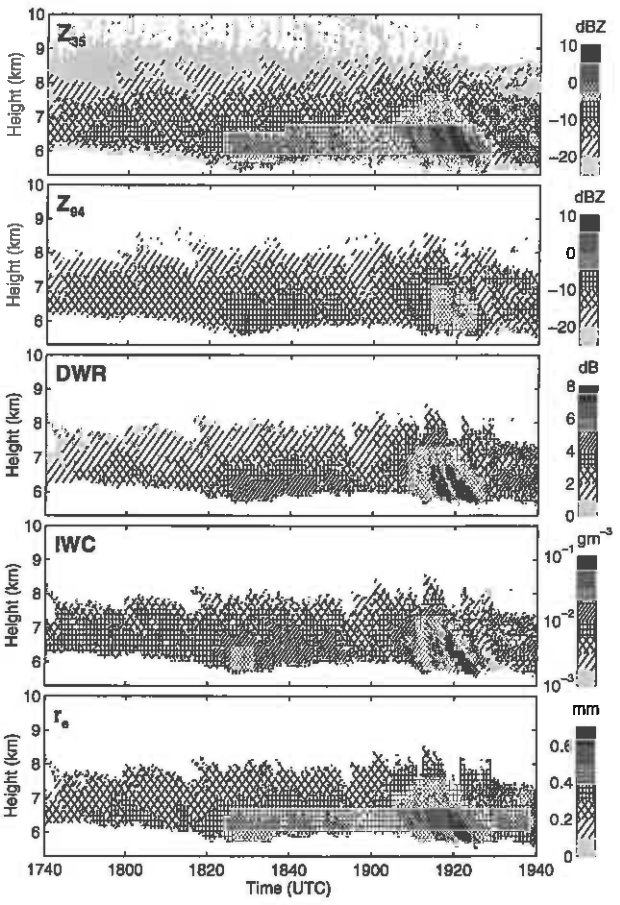

Figure 2: Time series of dual-wavelength radar data and derived quantities obtained on 22 June 1996: (from top) 35 GHz reflectivity factor; 94 GHz reflectivity factor; Dual Wavelength Ratio; Ice Water Content; effective radius.

* *Corresponding author address:* Robin J. Hogan, Department of Meteorology, University of Reading, Earley Gate, PO Box 243, Reading RG6 6BB, UK; e-mail: R.J.Hogan@reading.ac.uk.

obtained for r_e. Figure 1b shows how f varies with *DWR* for the each of the three cases, and it appears that the density of the large crystals has only a small effect on derived *IWC*. Estimates of total number density and cloud optical depth can then be found.

2 CASE STUDY

On 22 June 1996, dual-wavelength measurements were taken through thick cirrus. The antennae were vertically-pointing with a range gate spacing of 75 m, and Z was recorded as a 10 second average. Figure 2 shows a two hour time-height section of (unattenuated) Z at both wavelengths, *DWR*, and the derived quantities *IWC* and r_e for the second density function. The same data are presented in figure 3 as a scatterplot of *IWC* against Z_{35}, with lines of constant D_0 overlayed.

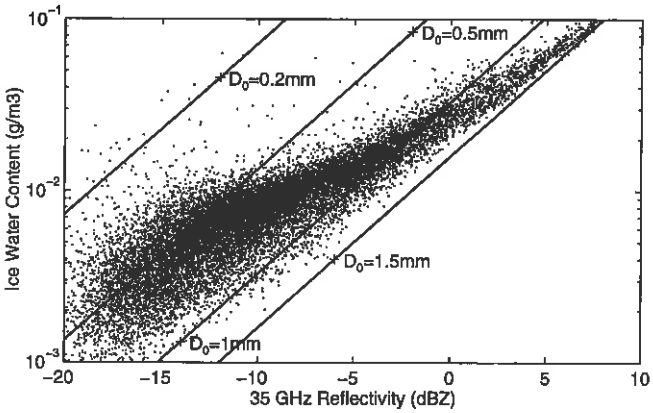

Figure 3: Scatterplot of Z_{35} against *IWC* for the data points which make up figure 2, with D_0 lines overlayed.

The 35 GHz radar has been calibrated by comparison with the 3 GHz radar at Chilbolton, and the small correction for gaseous attenuation has been made using thermodynamic data from the UK Meteorological Office (UKMO) Unified Model and the line-by-line model for millimeter-wave propagation of Liebe (1985). Attenuation by the ice crystals themselves can be neglected.

In theory *DWR* can be finely tuned by matching Z_{35} and Z_{94} in the Rayleigh-scattering cloud top, but it is clear from figure 2 that the 94 GHz radar is around 10 dB less sensitive than the 35 GHz radar (a problem that will be rectified shortly when the instrument is Dopplerized) and cannot detect cloud top. Together with the random error in *DWR* at low signal-to-noise ratios, a certain amount of uncertainty has been introduced into our size measurements, but this situation should be much improved in future observations with both radars sensitive down to −25 dBZ at 10 km. Even with improved accuracy however there is a limit to the effectiveness of this technique at very small sizes; it can be seen from figure 1 that in the presence of the smaller crystals both derived *IWC* and D_0 are much more sensitive to small changes in *DWR*.

It is expected that many of the uncertainties surrounding the assumptions we have had to make will be resolved in September-October 1997 when the UKMO C-130 aircraft will be available for concurrent microphysical probe and dual-wavelength radar measurements.

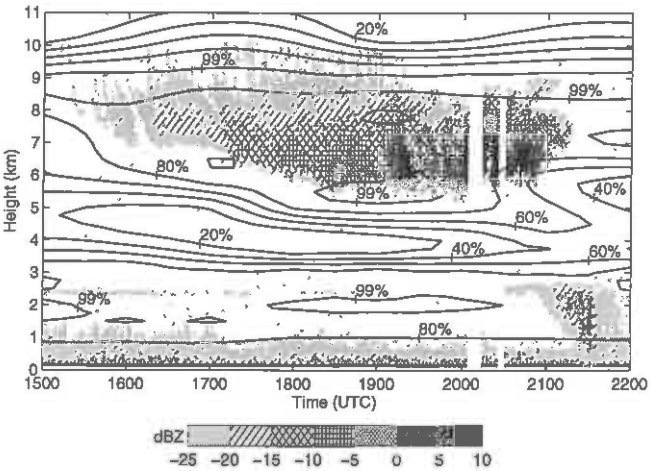

Figure 4: UKMO Unified Model relative humidity and 35 GHz reflectivity factor, for the period during which the cloud was overhead.

Figure 4 indicates the perfomance of the mesoscale version of the UKMO Unified Model at locating the whole cloud. The saturated cloud-filled region is clearly present, and the very dry air beneath is consistent with the sharpness of the observed cloud base, although the model has positioned it about a kilometer too low.

3 CONCLUSIONS

We have demonstrated the potential of this technique to make remote, high resolution measurements of both cloud Ice Water Content and crystal size. After validating the method by comparison with in situ aircraft observations, a month-long campaign is planned to objectively assess the representation of cirrus in both the UKMO and the ECMWF models.

ACKNOWLEDGEMENTS

We are grateful to RAL for the use of the Chilbolton radars. This research was funded by grants from NERC (GR3/8765), ESTEC (10568/95/NL/NB) and CEC (EV5V-CT94-0463).

REFERENCES

Brown, P. R. A. and P. N. Francis, 1995: Improved measurements of the ice water content in cirrus using a total-water probe. *J. Atmos. Oceanic Tech.*, **12**(2), 410–414.

Brown, P. R. A., A. J. Illingworth, A. J. Heymsfield, G. M. McFarquhar, K. A. Browning and M. Gosset, 1995: The role of spaceborne millimeter-wave radar in the global monitoring of ice-cloud. *J. Appl. Met.*, **34**(11), 2346–2366.

Liebe, H. J., 1985: An updated model for millimeter-wave propagation in moist air. *Radio Science*, **20**(5), 1069–1089.

Matrosov, S. Y., 1993: Possibilities of cirrus particle sizing from dual-frequency radar measurements. *J. Geophys. Res.*, **98**(D11), 20,675–20,683.

7B.4 A BISTATIC RADAR SYSTEM USING AN INCOHERENT TRANSMITTER

by J. D. Eastment [1]*, T. M. Blackman [2], I. N. Moore [1] and G. D. Aulich [2].

[1] Rutherford Appleton Laboratory, Chilton, Didcot, Oxfordshire, OX11 0QX. U.K.
[2] Department of Meteorology, University of Reading, Reading, Berkshire, RG6 2AU. U.K.

1. INTRODUCTION:

We describe the design and implementation of a novel, bistatic, coherent-on-receive meteorological Doppler radar for use with magnetron-based transmitters, which have random R.F. phase-angle from pulse-to-pulse. Previous systems [1],[2] have employed fully-coherent klystron transmitters, but, outside the U.S., most weather radar networks use magnetron transmitters, due to their reduced cost. This has provided the rationale for the development of a new variant of the bistatic Doppler technique, so that, in the future, it can be exploited in conjunction with existing operational radar networks.

The bistatic receiver reported here has been developed for operation with the Chilbolton S-band polarimetric Doppler radar ('CAMRa'). The engineering design of the timing and frequency synchronization circuitry, which is the key to the successful operation of the incoherent bistatic Doppler technique, is detailed.

As a demonstration of correct operation of our bistatic system, we present ray profiles and raster scans of reflectivity and Doppler velocity taken with the Chilbolton radar and the bistatic receiver, when the two systems were co-located and operated in pseudo-monostatic mode. These data confirm that, under appropriate conditions, close agreement is obtained between the monostatic radar and the bistatic system, in all measured parameters.

2. SYSTEM DESCRIPTION:

The existing Chilbolton radar STALO, COHO and system clock were all replaced with a new multiple-output frequency synthesizer. The radar was otherwise unchanged from its description in [3]. A second identical, but physically separate, synthesizer supplies the corresponding signals to the remote bistatic receiver. This unit is a conventional superhet, similar in design and performance to the Chilbolton radar receiver, with I.F. logarithmic amplifier video detector and I/Q detector. It is fed from a small, vertically-polarised horn antenna of 15 dBi gain. This horn, which is not optimal for the current application, but was available for initial tests, is inclined at an elevation of approximately half its -3 dB beamwidth, so as to improve the rejection of ground-clutter. The calculated sensitivity of the bistatic system is such that a 16 dBZ distributed target at 10 km range produces a signal-to-noise-ratio (SNR) of 0 dB. A block-diagram of the bistatic receiver is shown in Fig. 1.

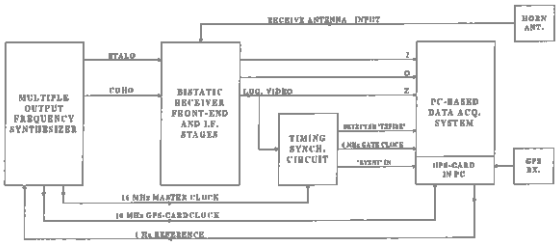

Fig. 1 - Bistatic radar receiver

The synthesizer unit (Fig. 2) will now be described in detail. The Global Positioning System (GPS) was chosen as a convenient and economical source of suitable time and frequency reference signals, which may be received on a world-wide basis. A phase-locked loop (PLL), with a phase comparator using the 1 Hz GPS time-signal as a reference, phase-locks a low phase-noise 10 MHz temperature-stabilized VCXO via a digital divider chain. A 12 bit quantized sample-and-hold circuit, based on a cascaded ADC/DAC combination, is used to combat DC drift in the loop filter. The requirement for a highly-stable VCXO control voltage, combined with the low phase-comparator reference frequency, means that this drift would otherwise present a problem.

The PLL's loop-bandwidth is very narrow, so that thermal and ageing effects only are compensated, and the inherently good close-to-carrier phase-noise performance of the high-quality crystal oscillator is not degraded. This is vital, as the 10 MHz signal is subsequently multiplied to S-band, for use as a STALO. The STALO spectral purity is an important determinant of radar system Doppler performance. A disadvantage of this approach is the rather long PLL lock-acquisition time, of the order of 2 days, but this is not a major concern in the current application.

The buffered 10 MHz squarewave outputs from the PLL unit, now phase-locked to GPS, are fed to three separate circuits, which produce the following signals:

COHO: The 30 MHz signal required as COHO injection for the receiver's I/Q detector is produced by bandpass filtering the 10 MHz squarewave at 30 MHz to select the appropriate harmonic component, followed by amplification to the correct level.

System Clock: The 16 MHz signal required as the data-acquisition system master clock is generated by digitally dividing the 10 MHz squarewave by 5, to produce 2 MHz, followed by multiplication by 8 in a series of three cascaded frequency doublers, each based on a diode double-balanced mixer with inter-stage filtering and amplification.

* *Corresponding author address*: J. D. Eastment, Building R25, Rutherford Appleton Laboratory, Chilton, Didcot, Oxon., OX11 0QX, U. K. (e-mail: j.d.eastment@rl.ac.uk).

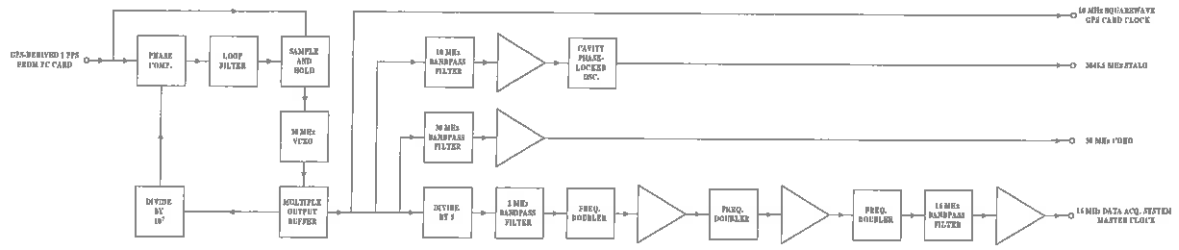

Fig. 2 - Frequency synthesizer unit

STALO: The 3046.5 MHz signal, required by the receiver to down-convert from the 3076.5 MHz transmitter frequency to the system I.F. of 30 MHz, is produced by a commercial cavity-oscillator based PLO, fed with a 10 MHz sinewave reference. The 10 MHz sinewave reference is produced from the GPS phase-locked squarewave by bandpass filtering and amplification.

The 10 MHz squarewave itself is also fed to a commercial GPS card in the PC, where it is used as the clock for a counter-timer circuit, which records the time-of-occurrence of each transmitter pulse.

Whilst frequency synchronization of all oscillators in each receiver is fundamental to proper bistatic Doppler operation, time synchronization is also necessary in this system to prevent uncertainties in range-gate position in space. This is because the Chilbolton radar employs a mechanical polarisation switch, based on a motor-driven rotary vane. In this system, inter-pulse periods (IPP) are determined by the rate of rotation of the vane, which is subject to small variations due to friction, motor power supply fluctuations and dish motion. Because these variations are a tiny fraction of the nominal IPP, they have a negligible effect on the measured Doppler velocities. However, the timing uncertainties introduced could cause a significant error in estimating target range, if it is simply assumed that the IPP is constant.

Range uncertainty in the monostatic (Chilbolton) radar is removed by synchronizing the 'transmit fire' signal to the next rising edge of the 4 MHz ADC range-gate clock after the rotary vane has reached its correct position. This ADC range-gate clock is derived from the 16 MHz master clock by division by 4.

The temporal synchronization problem for the remote bistatic receiver is, however, more complex, as there is no direct access to the 'transmit fire' signal. The solution adopted relies on detection at the bistatic receiver of the leading-edge of the microwave pulse emitted by the transmitter. In order for this approach to work reliably, the receiver must be within line-of-sight of the transmitter. As the monostatic radar antenna scans, the energy received at the bistatic antenna (which has travelled along the minimum propagation-delay straight-line path joining the two antennas), fluctuates as the maxima and minima of the monostatic radar antenna's polar diagram successively illuminate the receiver. Provided that the nulls in the monostatic radar antenna pattern are insufficiently deep so as to cause a loss of reception of the transmit pulse at the receiver (as, in practice, is found to be the case), detection is possible.

Although the magnitude of the log. video pulse, due to line-of-sight reception of the transmitter at the bistatic receiver, will vary considerably, the time delay between its rising edge and the rising edge of the monostatic radar's 'transmit fire' signal will be constant at $T = (d/c)+\Delta t$, where c is the speed of light, d is the antenna spacing, and Δt is a short, constant delay, due to the electronic circuitry. The delay Δt is easily measured, and T is determined from the bistatic system geometry.

This scheme is implemented in our bistatic receiver as shown in Fig. 3. A pair of comparators, C1 and C2, are used to inspect the amplitude of the receiver's log. video waveform. C1's threshold is set such that it is triggered by any signal level equal to or greater than that received from the transmitter via the minimum-delay path when the transmit antenna presents its deepest nulls in the direction of the receiver. This ensures detection of the transmitter pulse via the direct path for all transmit antenna pointing angles. (Note, however, that C1 may be re-triggered by any meteorological or ground-clutter echoes of sufficient amplitude, so we cannot use C1's output alone as an unambiguous indicator of transmitter pulse reception.)

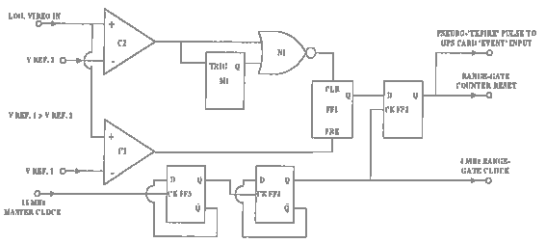

Fig. 3 - Timing synchronization circuitry

C2's threshold is set such that it is triggered by any signal level which exceeds the receiver thermal noise floor by more than 5 dB. Thus, it is triggered by all echoes corresponding to the meteorological targets of interest which have useable SNR's.

Because the weather targets may be discontinuous in range, that is, the log. video signal may fall to the thermal noise level in between discrete scattering cells, C2's output is used to fire a re-triggerable monostable, M1. The outputs of C2 and M1 are combined in NOR gate N1. With suitable choice of M1's time-constant, the rising-edge of N1's output may be used to indicate, with high confidence (the rare exception is a very high reflectivity target at a range corresponding to a large fraction of the IPP - typically a distant aircraft), that all weather echoes have died away. After this condition becomes valid, we may be certain that

the next time C1 is triggered corresponds to the reception of the leading edge of a new transmitter pulse.

Consequently, we use the outputs from C1 and N1 to preset and clear, respectively, an edge-triggered D-type flip-flop, FF1. The rising-edge of the output from this flip-flop is synchronized with the 4 MHz ADC range-gate clock in a further D-type, FF2, and the resulting output pulse is used as the reset signal for the bistatic receiver's range-gate counter. An error-flagging circuit monitors the apparent IPP to verify correct operation of the pulse detection scheme. These measures ensure that the physical sample volumes corresponding to the monostatic and bistatic range-gates neither drift nor jitter in space in an absolute sense, nor relative to each other. An added benefit of this technique is that this receiver system may be used in conjunction with a monostatic radar employing staggered PRF.

With the exception of the specialized frequency and timing signal generation detailed above, the remainder of the bistatic receiver's data acquisition system is conventional. Three 8-bit, 2 MHz ADC channels are used to digitize the Z, I and Q time-series for each range-gate of interest, and these data are written to a 64 M-byte block of RAM in the host PC. Every received transmitter pulse is tagged with a corresponding time using the 'EVENT' input of the GPS PC card. The contents of the RAM are subsequently copied to hard disk for off-line analysis, in conjunction with the corresponding data-set from the Chilbolton radar, where the Z, I and Q data are similarly time-tagged and recorded.

Analysis involves associating the corresponding range-gates due to a particular transmit pulse between the two data-sets by means of their GPS time-tags. The phase-angles due to target motion alone are determined for both sets of range-gates by removing the transmitter's random phase contribution, by angular subtraction, using the recorded values of down-converted transmitter pulse phase-angle from the monostatic radar's data-set.

This results in two sets of coherent-on-receive Doppler (and reflectivity) data, one for the monostatic radar and one for the bistatic receiver. These may be further processed to obtain, for example, a 2-dimensional wind-velocity field. However, in our experiment, the primary goal was to demonstrate the viability of this new incoherent bistatic technique. The most convincing proof of correct operation is obtained when the bistatic system is operated in a pseudo-monostatic configuration, since in-situ verification of radar-derived velocity estimates is not easily obtained for the sample-volumes of a true bistatic geometry. Under pseudo-monostatic conditions, the reflectivity and velocity estimates from the monostatic and bistatic systems should be comparable. Results of such an experiment are reported below.

3. RESULTS AND INTERPRETATION:

Test data were recorded during the passage of a small convective rain-cell through the observing area. Figs. 4 and 5 show comparisons of reflectivity and mean-velocity estimates, respectively, as a function of radial range along a particular ray. Figs. 6 and 7 depict a similar comparison for a sector-scan PPI. In both cases, the Chilbolton radar's 25 meter diameter dish, which has a 2-way, -3 dB beamwidth of 0.2° and corresponding 1-way, -3 dB beamwidth of 0.28°, was scanning in azimuth at a fixed elevation of 1°. The -3 dB E and H-plane beamwidths of the bistatic receiver's horn antenna are both 35°, and its azimuth pattern maximum was aligned with that of the dish at the central azimuth of the PPI.

Consequently, the bistatic reflectivity estimates in Fig. 6 would be expected to agree with those from the monostatic radar at and around the central azimuth of the PPI, but to be increasing underestimates as the edges of the 50°-wide scan are approached. This is clearly the case in the figure, and bistatic receiver SNR falls to unusable values at the margins of the PPI.

There are several reasons as to why the monostatic and bistatic mean-velocity estimates might not always be expected to be equal. These relate to the differences between the two systems in reception from the illuminated sample-volumes, due to the markedly different antenna patterns, and the inherently greater susceptibility of the bistatic measurements to sidelobe-clutter contamination, due to the fact that there is only 1-way, rather than 2-way, suppression of the monostatic radar antenna sidelobes relative to its main lobe.

The measured bistatic data show that at short ranges, sidelobe-illuminated ground-clutter returns dominate over the meteorological target Doppler signature, while at long ranges, there is inadequate SNR for satisfactory velocity determination. However, in the intermediate region, mean-velocity estimates are mostly in very good agreement with those of the monostatic radar. This is the proof-of-concept of the incoherent bistatic Doppler technique which was sought.

4. CONCLUSION AND FUTURE WORK:

A novel, low-cost approach to realizing a bistatic weather radar receiver system, based on the commonly-used incoherent magnetron transmitter, has been successfully demonstrated. In the future, this equipment will be deployed remotely from the Chilbolton site for a campaign of true-bistatic Doppler radar observations on precipitation.

5. REFERENCES:

[1] Wurman, J., Randall, M., Frush, C. L., Loew, E., and Holloway, C. L.: 'Design of a bistatic dual-Doppler radar for retrieving vector winds using one transmitter and a remote low-gain passive receiver', Proc. IEEE, December, 1994, Vol. 82, No. 12, pp 1861-1872.

[2] Wurman, J.: 'Vector winds from a single-transmitter bistatic dual-Doppler radar network', Bull. Amer. Meteorological Soc., 1994, Vol. 75, pp 983-994.

[3] Goddard, J. W. F., Eastment, J. D., and Thurai, M.: 'The Chilbolton Advanced Meteorological Radar: a tool for multi-disciplinary atmospheric research', IEE Electronics and Communication Engineering Journal, April 1994, Vol. 6, No. 2, pp 77-86.

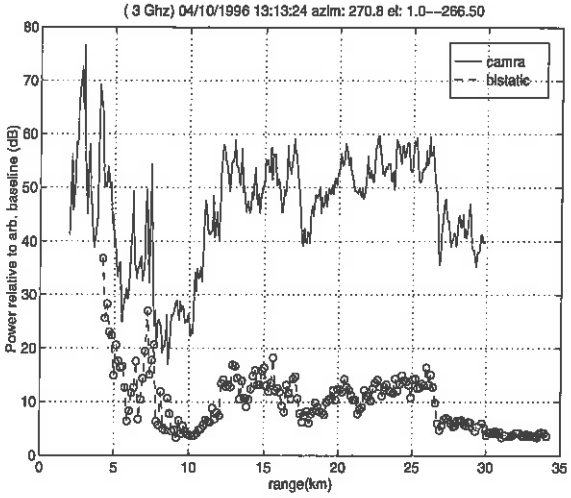

Fig. 4 - Reflectivity profile comparison along a ray

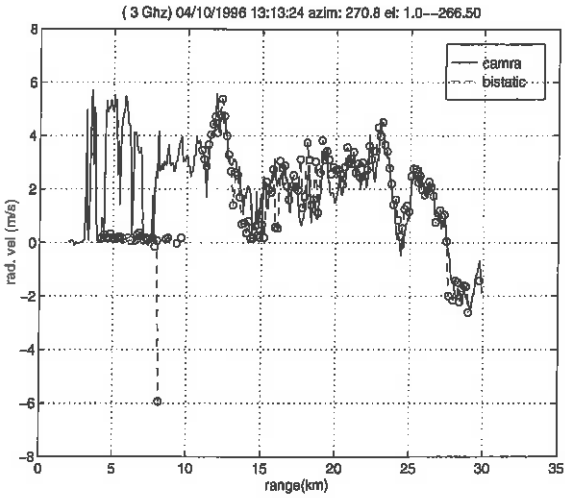

Fig. 5 - Mean velocity profile comparison along a ray

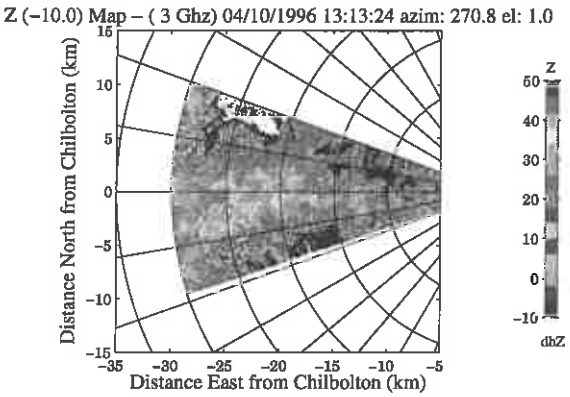

Monostatic

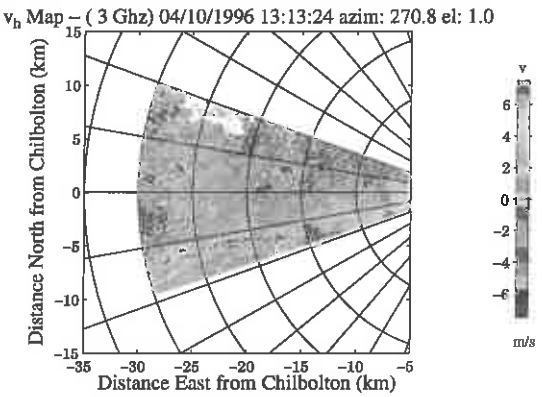

Monostatic

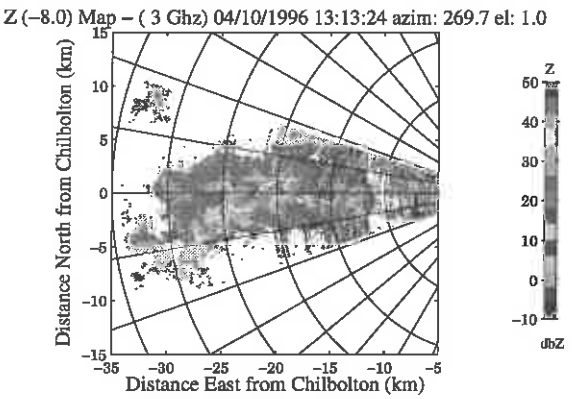

Bistatic

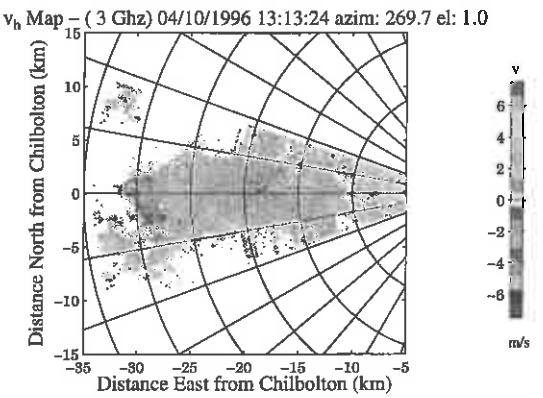

Bistatic

Fig. 6 - Reflectivity comparison for PPI scan

Fig. 7 - Mean velocity comparison for PPI scan

CURRENT JCMM INTERNAL REPORTS

This series of JCMM Internal Reports, initiated in 1993, contains unpublished reports and also versions of articles submitted for publication. The complete set of Internal Reports is available from the National Meteorlogical Library on loan, if required.

1. **Research Strategy and Programme.**
   K A Browning et al
   January 1993

2. **The GEWEX Cloud System Study (GCSS).**
   GEWEX Cloud System Science Team
   January 1993

3. **Evolution of a mesoscale upper troposheric voriticity maximum and comma cloud from a cloud-free two dimensional potential vorticity anomaly.**
   K A Browning
   January 1993

4. **The Global Energy and Water Cycle**
   K A Browing
   July 1993

5. **Structure of a midlatitude cyclone before occlusion.**
   K A Browning and N Roberts
   July 1993

6. **Development in Systems and Tools for Weather Forecasting**
   K A Browning and G Szejwach
   July 1993

7. **Diagnostic study of a narrow cold frontal rainband and severe winds associated with a stratospheric intrusion.**
   K A Browning and R Reynolds
   August 1993

8. **Survey of perceived priority issues in the parametrizations of cloud-related processes GCMs**
   K A Browning
   September 1993

9. **The Effect of Rain on Longwave Radiation**
   I Dharssi
   September 1993

10. **Physical Cloud Microphyrocesses - A Description of the Parametrization used in the Large Eddy Model.**
H Swann
July 1994

11. **An Appreciation of the Meteorlogical Research of Ernst Kleinschmidt.**
A J Thorpe
May 1992

12. **Potential Vorticity of Flow Along the Alps**
A J Thorpe, H Volkert and Dietrich Heimann
August 1992

13. **The Representation of Fronts.**
A J Thorpe
January 1993

14. **A Parametrization Scheme for Symmetric Instability: Test for an Idealised Flow.**
C S Chan and A J Thorpe
February 1993

15. **The Fronts 92 Experiment: a Quicklook Atlas**
Edited by T K Hewson
November 1993

16. **Frontal wave satability during moist deformation frontogenesis.**
Part 1. Linear wave dynamics
C H Bishop and A J Thorpe
May 1993

18. **Gravity waves in sheared ducts**
C Bishop and A J Thorpe
November 1993

19. **Potential Vorticity and Electroastatics Analogy: Quasi - Geostrophic Theory.**
C Bishop and A J Thorpe
November 1993

20. **Recent Advances in the Measurement of Precipitation by Radar.**
A J Illingworth - April 1993

21. **Micro-Physique et Givrage. Cloud Microphysics and Aircraft Icing.**
A J Illingworth May 1993

22. **Differential Phase Measurements of Precipitation.**
M Blackman and A J Illingworth
May 1993

23. **Estimation of Effective Radius of Cloud Particles from the Radar Reflectivity.**
N I Fox and A J Illingworth
May 1993.

24. **A Simple Method of Dopplerising a Pulsed Magnetron Radar.**
A Hau, A J Illingworth and J Eastment
November 1993.

25. **Radiation and Polar Lows.**
George C Craid
February 1994

26. **Collected preprints submitted International Symposium on the life Cycles of Ectratropical Cyclones; Bergen, Norway, 27 June - 1 July 1994**
April 1994.

27. **Convective Frontogenesis**
Douglas J Parker and Alan J Thorpe
April 1994

28. **Improved Measurement of the Ice Water Content in Cirrus Using a Total Water Evaporator.**
Philip R A Brown and Peter N Francis
April 1994

29. **Mesoscale Effects of Dry Intrusion within a vigorous Cyclone**
K A Browning and B W Golding
April 1994

30. **GEWEX Cloud System Study, Science Plan**
May 1994

31. **Parametrization of Mometum Transport by Convectively Generated Gravity Waves.**
R Kershaw
February 1995

32. **Mesoscale Modelling Newsletter, No5.**
May 1994

33. **Observations of the mesoscale sub-structure in the cold air of a developing frontal cyclone.**
K A Browning, S A Clough, C S A Davitt, N M Robertsf and T D Hewson
May 1994

34. **Longwave Radiative Forcing of a Simulated Tropical Squall Line**
Imtiaz Dharssi
July 1994

35. **On the nature of the convective circulation at a Kata-cold front**
K A Browning
September 1994

36. **Collective preprints of papers submitted to the COST-75 International Seminar on Advanced Weather Radar Systems, Brussels, 20-23 September 1994.**
November 1994

37. **Use of satellite imagery to diagnose events leading to frontal thunderstorms: Parts 1 and 11 of a case study.**
K A Browning and N M Roberts
November 1994

38. **The role of spaceborne millimeter-wave radar in the global monitoring of ice cloud.**
P R A Brown, A J Illingworth, A J Heymsfield, G M McFarquahar, K A Browning and M Gosset.
December 1994

39. **Potential Vorticity Inversion**
Michael Ziemianski
October 1994

40. **Theory of mature tropical cyclones; A comparison between Kleinschmidt (1951) and Emanual (1986)**
Suzanne L Gray
December 1994

41. **Dispersion and removal of pollutants during the passage of an atmospheric frontal System.**
N R Gimson
December 1994

42. **The role of snow sublimation in frontogenesis**
D J Parker and A J Thorpe
December 1994

43. **Potential vorticity and the electrostatics Analogy: Ertel- Rossby formulation**
A J Thorpe and C H Bishop
December 1994

44. **Mesoscale aspect of extratropical cyclones: and observational perspective**
K A Browning
January 1995

46. **Generation of near-surface gusts of deep convection**
K Nakamura and R Kershaw
April 1995

47. **Attribution concepts applied to the Omega Equation**
S A Clough, C S A Davitt and A J Thorpe
June 1995

48. **Parametrization of mixed-phase cloud and precipitation**
Susan P Ballard and M Gerard Hutchinson
June 1995

49. **Short-range forecasting of stratocumulus: Initialization V Prediction**
Susan Ballard, Simon D Jackson and B Macpherson
June 1995

50. **Contribution of the JCMM/Dept of Meteorology Radar Group to the 27th AMS Radar Meteorology Conference, Vail October 1995.**
June 1995

51. **Cold pools in shear**
Douglas J Parker
September 1995

52. **High-resolution analysis of frontal fracture**
K A Browning, S P Ballard and C S A Davitt
September 1995

53. **The Albedo of Broken Cloud Fields: Calculations using a modified two stream radiation code.**
Imatiaz Dharssi and Roy Kershaw
October 1995

54. **Parametrization of momentum transport by convection. I: Theory and cloud modelling results.**
P Kershaw and D Gregory
November 1995

55. **Variation of frontal structure along a cold front**
K A Browning and N M Roberts
November 1995

56. **Secondary Frontal Waves**
Douglas Parker
December 1995

57. **Objective Fronts**
T D Hewson
March 1996

58. **Mesoscale analysis of the activation of a cold front during cyclogenesis**
K A Browning, N M Roberts and A J Illingworth
June 1996

59. **Investigation of different representations of rain in a 1-d evaporation model**
H Swann
May 1996

60. **Parametrization of diabatic processes in the inversion of the omega-equation**
M Athanassiadou and A J Thorpe

61. **The role of the environmental flow in the development of secondary frontal cyclones.**
I A Renfrew, A J Thorpe and A Joly
June 1996

62. **Contributions to the AMS/RMS Conference on Mesoscale Processes Reading**
S Malardel, A J Thorpe and A Joly
June 1996

63. **Contributions to the AMS/RMS Conference on Mesoscale Processes Reading.**
9-13 September 1996
June 1996

64. **Vorticity and Potential Vorticity Stratified Flows Interacting with an Isolated Obstacle.**
Jorge A Gutierrez and A J Thorpe - September 1996

65. **Triple Point Development: Two Case Studies**
Douglas Parker
September 1996

66. **Radar observations of wind-shear splitting within evolving atmospheric Kelvin-Helmholtz billows**
D. Chapman and K.A.Browning
April 1997

67. **Cold Frontal Structure derived from radar wind profilers**
K.A.Browning, D. Jerrett, J.Nash, T.Oakley, N.M.Roberts
May 1997

68. **The dry intrision and its effect on the frontal, cloud and precipitation structure of extratropical cyclones**
K.A. Browning - Text of invited special lecture at the Spring Conference of the Meteorological Society of Japan, University of Tsukuba, 22 May 1997.

69. **Met. Office Unified Model data, diagnostic, graphics programs, and other observational data available from the JCMM through the aegis of the Universities Weather Research Network UWERN**. Plus supplement.
Peter Panagi and Ed Dicks
June 1997

70. **Contributions of the JCMM/Dept of Meteorology Radar Group to 28th AMS Radar Meteorology Conference.** Austin, Texas, September 1997

Met Office Joint Centre for Mesoscale Meteorology Department of Meteorology
University of Reading PO Box 243 Reading RG6 6BB United Kingdom
Tel: +44 (0)118 931 8425 Fax: +44 (0)118 931 8791
www.metoffice.com